Polyethylene Hydrogenolysis at Mild Conditions over Ruthenium on Tungstated Zirconia

Cong Wang, Tianjun Xie, Pavel A. Kots, Brandon C. Vance, Kewei Yu, Pawan Kumar, Jiayi Fu, Sibao Liu, George Tsilomelekis, Eric A. Stach, Weiqing Zheng, and Dionisios G. Vlachos*

ABSTRACT: Plastics waste has become a major environmental threat, with polyethylene being one of the most produced and hardest to recycle plastics. Hydrogenolysis is potentially the most viable catalytic technology for recycling. Ruthenium (Ru) is one of the most active hydrogenolysis catalysts but yields too much methane. Here we introduce ruthenium supported on tungstated zirconia (Ru-WZr) for hydrogenolysis of low-density polyethylene (LDPE). We show that the Ru-WZr catalysts suppress methane formation and produce a product distribution in the diesel and wax/lubricant base-oil range unattainable by Ru-Zr and other Ru-supported catalysts. Importantly, the enhanced performance is showcased for real-world, single-use LDPE consumables. Reactivity studies combined with characterization and density functional theory calculations reveal that highly dispersed $(WO_x)_n$ clusters store H as surface hydroxyls by spillover. We correlate this hydrogen storage mechanism with hydrogenation and desorption of long alkyl intermediates that would otherwise undergo further C−C scission to produce methane.

KEYWORDS: plastic waste, hydrogenolysis, low-density polyethylene, ruthenium, tungstated zirconia, hydrogen spillover

INTRODUCTION

Over 12 billion tons of plastic waste are projected to end in landfills or leak into the environment by 2050.[1] Roughly 60% of the global plastics are polyolefins, such as polyethylene and polypropylene, whose recycling rates are currently too low.[2−4] The chemical composition and structure giving rise to the materials' desired properties, such as their stability, is the very reason their recycling is so challenging. Mechanical recycling and incineration are somewhat limited in scope for these plastics. Chemical recycling and specifically catalytic depolymerization is potentially attractive to combating polyolefin plastic waste.[5−12] Among approaches, catalytic cracking is facile, but it requires high reaction temperatures (typically above 673 K), and is prone to low-value gas products.[9,11,13−16] Olefin-mediated metathesis[17] has recently been applied to polyethylene decomposition using a large volume of pentane and long residence times.[6] Bifunctional hydrocracking has been proven feasible at moderate temperatures and H_2 pressures.[5,12,18−22] High branching imparts desirable properties to fuels and lubricants. However, it requires suitable catalysts to achieve appropriate metal−acid balance in strength and site density;[12] the rate-limiting acid functionality often impedes high activities at lower temperatures.

Metal-catalyzed hydrogenolysis has recently drawn significant attention due to its decent reactivity and selectivity at low temperatures. Prior work has focused on discovering hydrogenolysis catalysts to produce fuels for proof-of-concept.[6,8,23−26] For example, the hydrogenolysis of polyethylene over an ordered mesoporous shell/active site/core, Pt/SiO_2 catalyst was showcased to demonstrate a processive mechanism.[27] Ruthenium-supported catalysts, e.g., Ru/C,[24,26,28] Ru/zeolites,[29] and Ru/CeO_2,[23] possess higher activity than Pt[8,25] and are potentially promising materials. Unfortunately, Ru generates significant methane, which is an undesirable, low-value product. Besides, most studies involve either a large catalyst-to-polymer ratio, long processing times, or solvents. Ultralow molecular weight plastics are commonly employed as substrates to enable high conversions at low temperatures.[23,24] While exciting initial results have been obtained, there is a clear need for more active and selective catalysts to enable practical implementation.

Here we demonstrate that ruthenium on tungstated zirconia (Ru-WZr) is highly active for the hydrogenolysis of low-density polyethylene (LDPE, molecular weight, Mw, ~76 kDa) at mild conditions (523 K and 50 bar H_2 for 2 h). The deconstruction rate is fast, although a direct comparison to previous contributions is impossible due to different
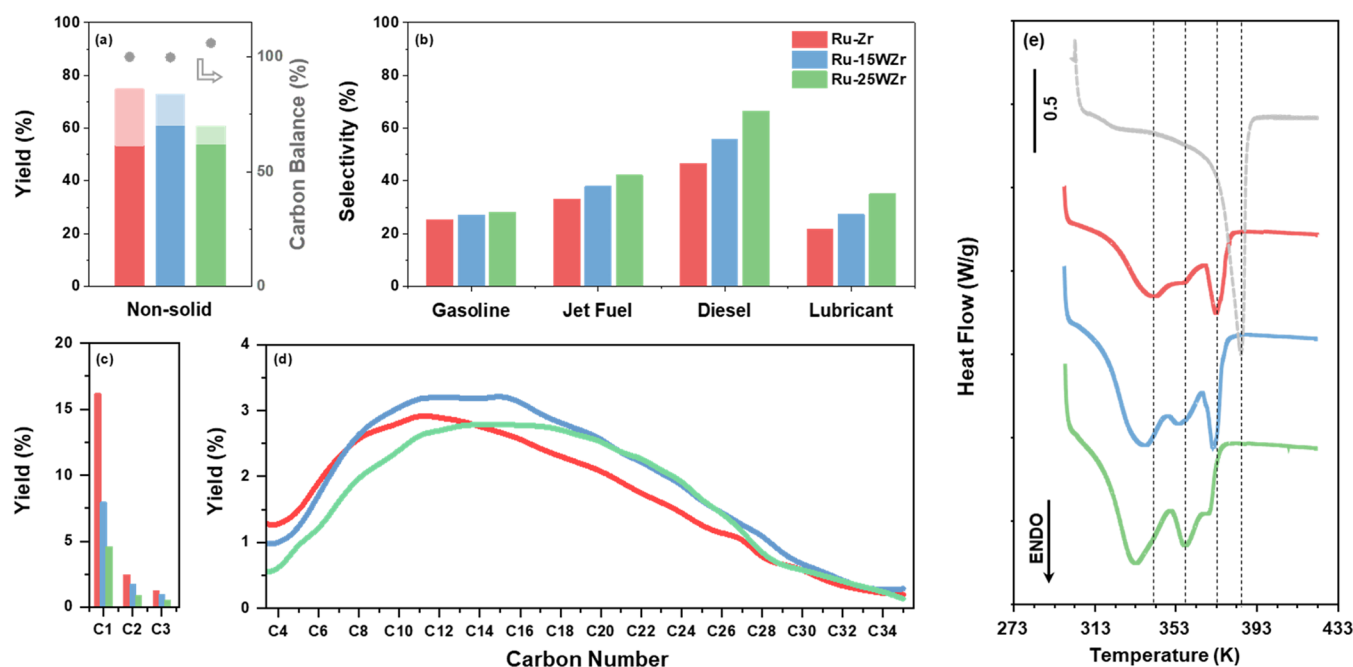
Figure 1. Effect of WO$_x$ incorporation in Ru-WZr catalysts on LDPE hydrogenolysis. Yields and selectivities for LDPE hydrogenolysis over Ru-Zr (red), Ru-15WZr (blue), and Ru-25WZr (green) catalysts. a, Carbon balance (gray dots), yields of soluble (solid bars), and gaseous (faded bars) products. b, Selectivities by fuel range: gasoline, C5−C12; jet fuel, C8−C16; diesel, C9−C22; and waxes/lubricant base-oils, C20−C35. c and d, Detailed carbon distributions of the nonsolid products. e, Differential scanning calorimetry curves of the solid product residues referenced to pristine LDPE (gray curve). Auxiliary lines at 342, 358, 373, and 385 K. Reactions performed at 523 K and 50 bar H$_2$ for 2 h with 2 g of LDPE and 50 mg of catalyst.

experimental conditions, substrates (especially regarding the large variability in molecular weight), and catalyst supports. Compared to Ru supported on bare zirconia (Ru-Zr), tungstated silica (Ru-WSi), HY zeolite (Ru-HY), and mesoporous [Al]MCM-41 (Ru-[Al]MCM-41) as benchmarks, the Ru-WZr catalyst significantly suppresses methane; it produces a heavier and more valuable carbon product distribution for fuel and wax/lubricant base-oil. We hypothesize that excessive methane is primarily made via cascade surface reactions when hydrogenation and desorption of long alkanes are rate-limiting. Extensive catalyst characterization and density functional theory (DFT) calculations demonstrate highly dispersed (WO$_x$)$_n$ clusters that increase the H storage capacity in surface hydroxyls by spillover from Ru to WO$_x$. We provide evidence for a strong correlation of the excess hydrogen storage and the hydrogenation of intermediates, possibly by reverse spillover, interfacial sites, and/or catalyst–polymer interactions and desorption from the catalyst to avoid significant cracking leading to small hydrocarbons and methane. The implications for the rational design of polyolefin hydrogenolysis catalysts are discussed.

RESULTS

LDPE Hydrogenolysis on Ru-WZr Catalysts

We first demonstrate the promotional role of WO$_x$ in Ru-WZr catalysts on the mild hydrogenolysis of low-density polyethylene (LDPE, Mw ∼ 76 kDa). The operating conditions are rather mild, namely, a relatively low temperature of 523 K (250 °C), ensuring depolymerization proceeds in the melt phase, a short processing time of 2 h, and a low amount of catalyst (polymer to catalyst mass ratio of 40).

Figure 1 compares the product distributions over Ru-Zr, Ru-15WZr, and Ru-25WZr catalysts (hereafter, the number in

front of W indicates the weight percent of the added WO$_3$). Overall, the catalysts are significantly active. The overall nonsolid (liquids plus gases) yield is relatively high given the mild conditions (Figure 1a: 75%, 73%, and 55%, respectively) and is similar among catalysts, Ru-25WZr is less active but more selective to heavy liquids. Figure 1a−d shows that WO$_x$ has a profound effect on product distribution at similar conversions. It effectively decreases the gas yield from 21 to 7% and the undesired methane yield from 16% to 4.6%. It consequently enhances the selectivity to liquids as follows: gasoline from 25% to 28%, jet fuel from 33% to 42%, diesel fuel from 47% to 66%, and wax/lubricant base-oil from 22% to 35%. The results obtained over Ru-15WZr were benchmarked by good performing catalysts, Ru−Ce and Ru−C, reported previously[23,24] (Figure S1 and the discussion in the Supporting Information). Effectively, the Ru-WZr catalysts shift the distribution to heavier, more valuable, soluble products (the peak of the distribution shifts from C11 to C15). We elaborate with extensive characterizations that the apparent reaction rate of the Ru-WZr catalysts is affected by the interplay of reduced Ru site density and an increased turnover frequency and is comparable to that on Ru-Zr. The key difference between catalysts (Figure 1) is in selectivity.

Differential scanning calorimetry (DSC) of the solid residue (Figure 1e) and pristine LDPE (melting temperature, T_m ∼ 385 K) shows that the leftover solid over Ru-Zr possesses a low-temperature broad feature centered at 342 K, a shoulder at 358 K, and a high-temperature sharp feature centered at 373 K. These features are assigned to C20−C35, C35−C50, and C50−C100 products, respectively.[30−33] The DSC features over Ru-15WZr and Ru-25WZr shift progressively to lower temperatures with increasing WO$_x$ loading, indicating a solid consisting of shorter chains. Conversely, the corresponding
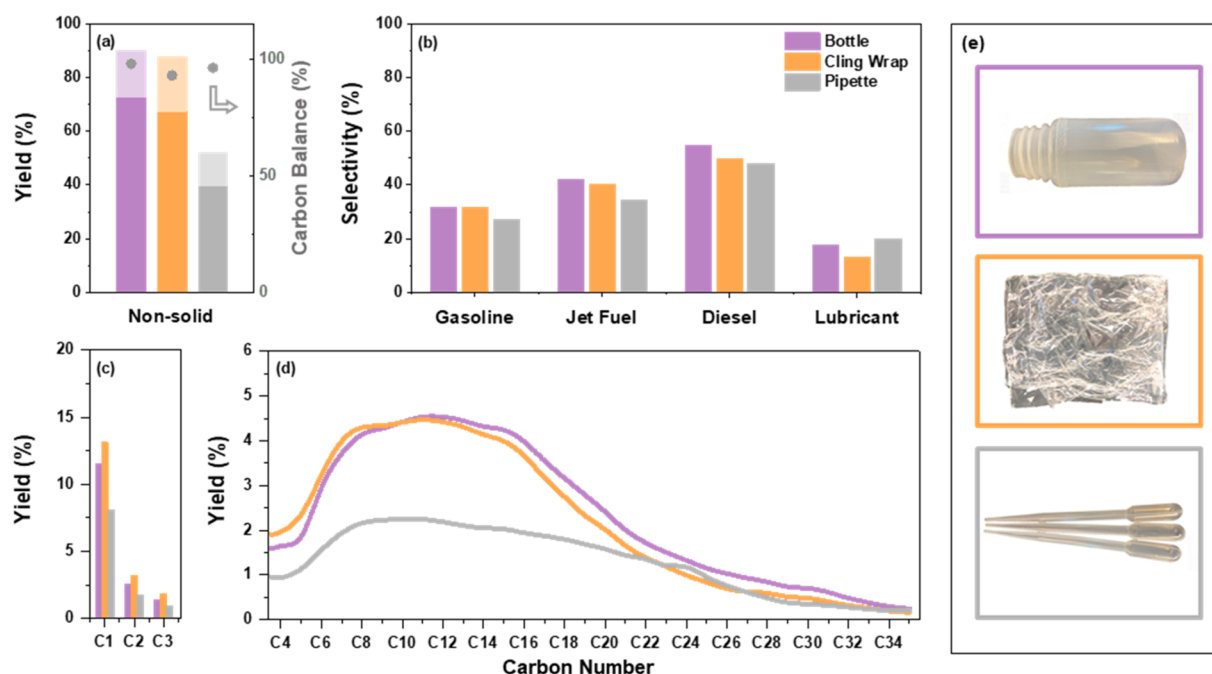
Figure 2. Hydrogenolysis of real-world consumable LDPE plastics over the Ru-15WZr catalyst. Yields and selectivities for hydrogenolysis of single-use LDPE bottle (purple), cling wrap (orange), and laboratory pipettes (gray) over the Ru-15WZr catalyst. a, Carbon balance (gray dots) and yields of soluble (solid bars) and gaseous (faded bars) products. b, Selectivities by fuel range: gasoline, C5−C12; jet fuel, C8−C16; diesel, C9−C22; and waxes/lubricant base-oils, C20−C35. c and d, Detailed carbon distributions of the nonsolid products. e, Images of the single-use plastics. Reactions performed at 523 K and 50 bar H_2 with 2 g of LDPE and 50 mg of catalyst for 2 h for the bottle, 1.5 h for the cling wrap, and 1.25 h for the pipettes to reduce the conversion to below 100% nonsolid yield.

nonsolid is heavier (Figure 1c,d), indicating a heavier carbon distribution of the products. Reduction in the melting temperature may also result from varying branching degrees;[34] we rule out this possibility due to forming mainly normal alkanes with low branching (Table S1). Excitingly, Figure 1 demonstrates that WO_x modification of the Ru-WZr catalysts can suppress methane formation and shift the carbon distribution to larger, value-added alkanes, such as diesel and wax/lubricant base-oils. WO_x modification overcomes an essential barrier of the otherwise excellent Ru catalyst reported in other works and does so at short times and low temperatures.

Excitingly, hydrogenolysis of real-world, single-use plastic consumables, such as LDPE bottles, cling wraps, and pipettes (Figure 2e), over the Ru-15WZr catalyst gave near quantitative conversion (Figure 2a), with selective product distributions (Figure 2b−d) similar to that of the pristine LDPE shown in Figure 1.
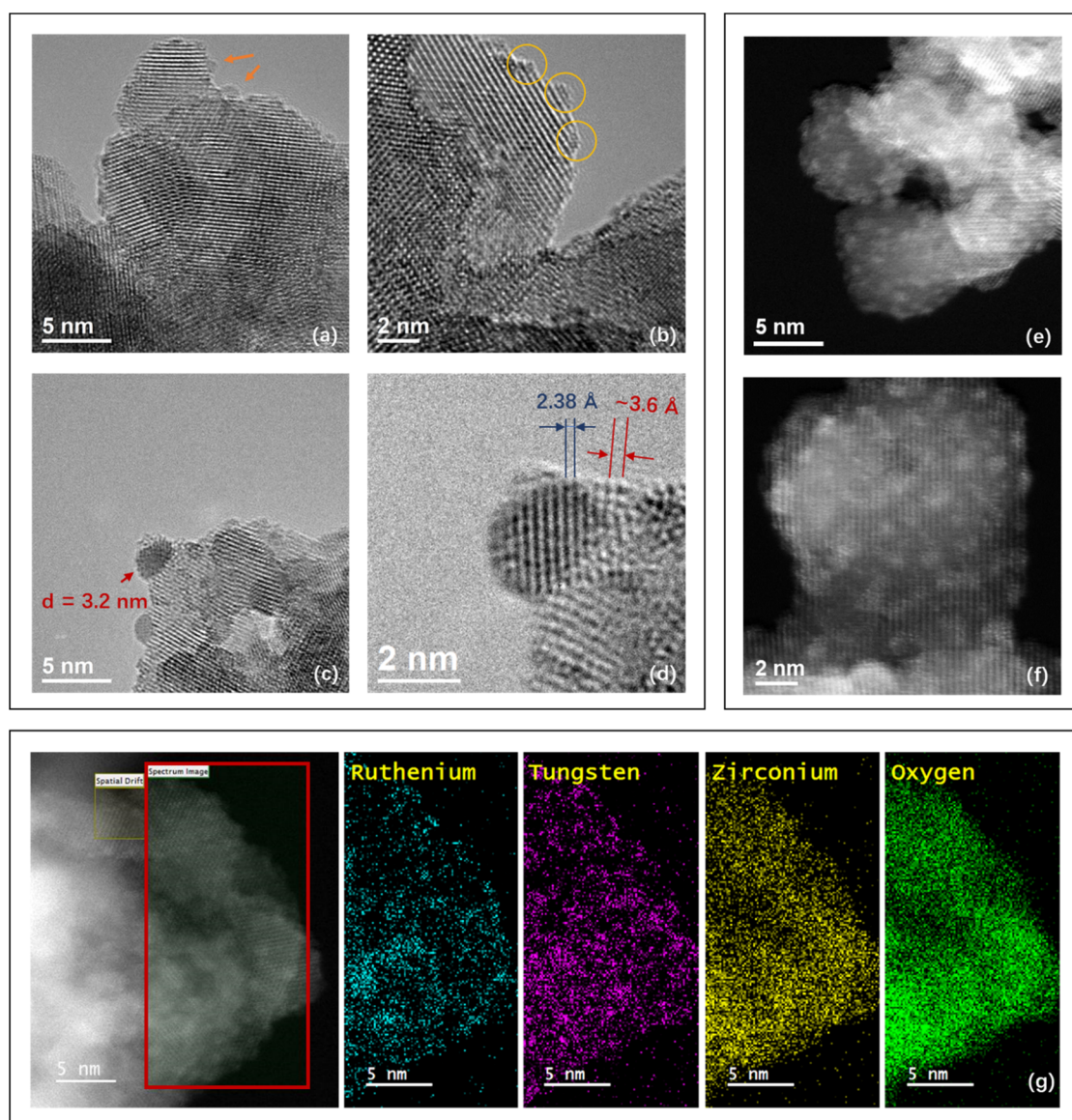
Structural Characterization of Ru-WZr Catalysts

High magnification BF-TEM, HAADF-STEM, and EDS elemental mapping of the Ru-15WZr (Figure 3) and Ru-Zr (Figure S2) catalysts shows that the Ru-Zr has a characteristic mesoporous structure of around 10 nm diameter (Figure S2a) and ∼1−5 nm Ru nanoparticles (Figure S2c,d) consistent with BET (Table S2) and H_2 titration data (Table S3). *In situ* EXAFS results (Table S4) show that the Ru−Ru coordination numbers of the reduced Ru-Zr and Ru-15WZr catalysts are 8.3 and 6.6, respectively, which indicate that the Ru particle size decreases on average only slightly with the WZr support.[35]

Distinguishing Ru from $(WO_x)_n$ in Ru-15WZr based on the TEM contrast is challenging due to similar atomic numbers. However, the surface roughness of Ru-15WZr (Figure 3a,b)

and Ru-Zr (Figure S2a,b) indicates that the highly dispersed ∼1 nm clusters in the former are most likely $(WO_x)_n$.[39] HAADF-STEM images (Figure 3e,f), XRD (Figure S3a), and STEM-EDS mapping (Figure 3g) further confirm the high dispersion of Ru nanoparticles and $(WO_x)_n$ clusters. Intriguingly, a Ru particle depicted in Figure 3c is partially covered with an overlayer, identified as a WO_x cluster, using the lattice parameter[36−38] (Figure 3d). This suggests that the $(WO_x)_n$ species are mobile[40] and may redisperse onto the metal of Ru during impregnation/reduction. Ambient temperature Raman spectra (Figure S3b) confirmed that the $(WO_x)_n$ species are highly amorphous and lack WO_3 crystalline structure in the presence of Ru. Furthermore, the HAADF-STEM data and EDS Ru and W maps shown in Figure 3g indicate that the two elements show substantial spatial overlap. These partial overlayers significantly decrease the Ru site density when increasing WO_x loading (Table S3). However, the LDPE reactivity on Ru-WZr catalysts does not decrease as much (Figure 1a), suggesting that WO_x enhances the Ru turnover rate.

The 15WZr sample has a WO_x surface density (∼6.6 W/nm², Table S2) corresponding close to a monolayer coverage.[41,42] WO_3 crystallites are nearly absent in the XRD or Raman spectra (Figure S4a,b). Unlike ZrO_2 with a tetragonal or monoclinic structure, ZrO_2 in 15WZr is predominantly tetragonal (Figure S4a). Characteristic Raman bands in ZrO_2 decrease significantly with increasing W loading (Figure S4b), suggesting a high WO_x coverage. The 25WZr sample has similar structural features except for WO_3 crystallites seen in XRD and Raman spectra (Figure S4a,b) due to a higher loading (∼10.7 W/nm², Table S2; more than one monolayer coverage). The 15WZr sample exhibits Brønsted acidity based on pyridine adsorption (Figure S4c), and Ru does not

Figure 3. Structural characterization of Ru-15WZr catalyst. a, TEM image of Ru-15WZr showing a rough surface consisting of Ru nanoparticles (arrows) and ~1 nm $(WO_x)_n$ clusters. b, High magnification image showing ~1 nm surface clusters (circles). c, Representative Ru hemispherical particle partially covered by an overlayer. d, High magnification image indicating a lattice spacing of 2.38 Å, consistent with Ru(100),[36] and a lattice spacing of ~3.6 Å of the overlayer, consistent with monoclinic WO_3.[37,38] e and f, DF-STEM images of Ru-15WZr indicating a uniform distribution of the ~1 nm WO_x clusters. g, STEM-EDS elemental mapping of the Ru-15WZr catalyst.

significantly affect the acidity of the 15WZr support (Figure S4d). However, the Ru-15WZr shows negligible isomerization activity (Table S1), suggesting a lack of metal−acid bifunctional hydrocracking−hydroisomerization chemistry. Compared to the bifunctional Pt-WZr catalyst we reported recently, which promotes a high degree of branching,[19,43] Ru is much more active for deep dehydrogenation and subsequent C−C scission due to stronger metal−carbon bond strength.[44,45] This prevents Ru from producing olefins that undergo hydrocracking and isomerization over the Brønsted acid sites.[46] Two additional Ru catalysts on highly acidic HY (Si/Al_2 = 30) zeolite and mesoporous [Al]MCM-41 (Si/Al_2 = 25) were prepared to understand the role of acidity. Moderate branching (Table S5) was observed, likely due to the stronger Brønsted acid strength[47] and much greater site density of these supports.[19] However, these catalysts are not as active (56% and 68% conversion over Ru-HY and Ru-[Al]MCM-41,

respectively) and produce much higher methane yields (36% and 52%, respectively) compared to Ru-15WZr under identical conditions. These findings suggest that acidity is not as critical a factor to methane suppression over the Ru-WZr catalysts.

Proposed Reaction Mechanism over Ru-WZr Catalysts

The time evolution for LDPE hydrogenolysis over Ru-15WZr is depicted in Figure 4. The data exhibits characteristic sequential reactions converting longer alkanes to shorter ones, evidenced by bell-shaped trajectories of C20+, C17−C19, and C13−C16 (longer molecules reach maxima at shorter times), with a monotonic growth of C8−C12, C5−C7, and C1−C4. The nonsolid products progressively shift toward lower molecular weights (Figure 4c,d). Methane becomes dominant (20% yield) only at long reaction times after severe overreaction due to the sequential nature of the reaction. Noticeably, the nonsolid yields experience a 10-fold increase from 7% to 73% between 1 to 2 h (Figure 4a). In this time
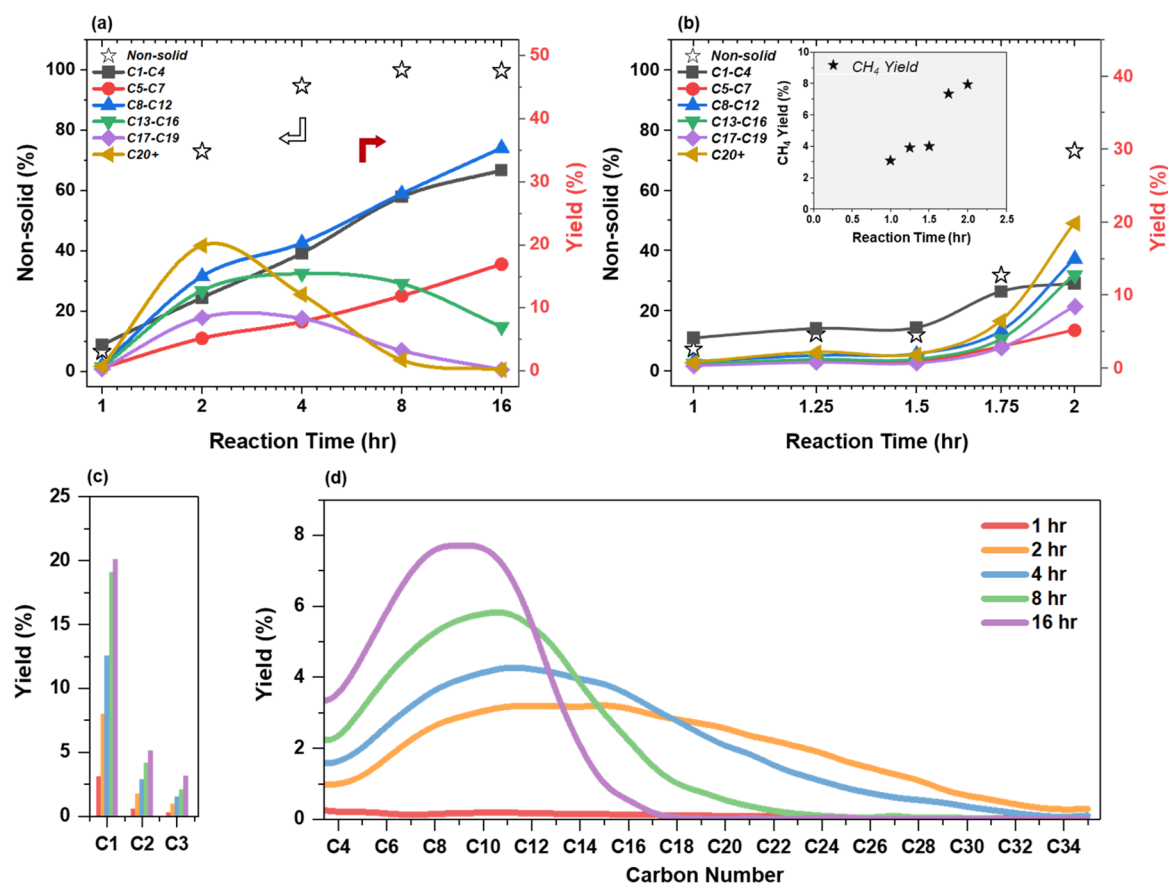
Figure 4. Reaction time analysis on Ru-15WZr. Time evolution of nonsolid yields in LDPE hydrogenolysis over Ru-15WZr catalysts. Reactions performed at 523 K and 50 bar H_2 for 1−16 h with 2 g of LDPE over 50 mg of catalyst. a, Yields at 1−16 h. b, Yields at 1−2 h; the inset shows the time evolution of methane yield. c and d, Detailed carbon distributions of the nonsolids at the times indicated.

interval, further experiments (Figure 4b) reveal a light-off in nonsolid yields between 1.5 and 1.75 h (from 12% to 32%). TEM images of postreaction (2 h) catalyst (Figure S5) show no noticeable morphological or size change in Ru and $(WO_x)_n$ clusters compared to the fresh sample (Figure 3a−d). No sudden changes in the solid DSC curves occur at this time interval (Figure S6), i.e., the melt of the LDPE is steadily depolymerized. This indicates the hydrogenolysis product distribution swiftly shifts to lower carbon numbers in the early stages of the reaction and becomes GC detectable in the C1−C35 carbon range after 1.5 h (Figure 4b). At 1 h, the yield of C1−C35 alkanes is only 7% (of which methane is 3%); during this time, the LDPE (Mw ∼ 76 kDa) is substantially decomposed to the ∼C300 range (estimated from the Mw of ∼4 kDa LDPE standard).

Notably, methane is produced in disproportionally large fractions early on (Figure 4b), and its yield increases relatively linearly with time (inset in Figure 4b), indicating its parallel production with the hydrogenolysis of long alkanes. Continuous flow hydrogenolysis experiments using *n*-hexane as a surrogate are consistent with this hypothesis (Figure S7, see discussion in Supporting Information), whereby methane forms via a cascade of multiple C−C bond scissions within one *n*-hexane turnover. Hereby, we propose that methane forms through a cascade hydrogenolysis mechanism illustrated in Scheme 1a. The first C−C bond scission (ii) is initiated following dehydrogenation (i).[44] The hydrogenation/desorption (iii) of reaction intermediates is rate-limiting, especially for long alkyls in hydrogen deficient environments. As a result,

these surface species undergo multiple C−C bond scissions (iv−v) before hydrogenation and desorption (vi). Since these intermediates are bound to the Ru surface with newly formed terminal carbons (ii), further C−C bond breaking favors demethylation to make methane (iv−vii). Ru catalysts favor terminal C−C bond breaking even in the primary C−C scission (i−iii).[48−50] The proposed cascade mechanism (iv−vii) must be invoked in the decomposition to rationalize the disproportionally high methane yields in both LDPE and model hexane reactions consistent with recent contributions.[24,29]

Catalytic performance at various hydrogen pressures supports this mechanism (Figures S8−S10, see detailed discussion in Supporting Information). Activities and selectivities (lower methane yield and heavier product distributions) increase over Ru-Zr and Ru-15WZr catalysts with increasing H_2 pressure. A higher H_2 pressure promotes the rate-limiting hydrogenation of intermediates followed by their desorption (iii), thereby enhancing the apparent rate and suppressing methane formation (iv−vii).

We hypothesize that the promotional effect of WO_x (Figure 1) may share the same origin as the hydrogen pressure. Indeed, the benefit of high H_2 pressure diminishes with increasing WO_x loading (Figure S10). At sufficiently high H_2 pressure, such as 130 bar, the hydrogenation/desorption (iii) step no longer limits the overall rate. The product distributions on Ru-Zr and Ru-15WZr become similar at comparable conversions (Figure S8g,h) with rates proportional to their Ru site density (123 and 76 μmol/g, respectively, Table S3). This suggests

**Scheme 1. Schematic of the Proposed Reaction Mechanisms[a]**
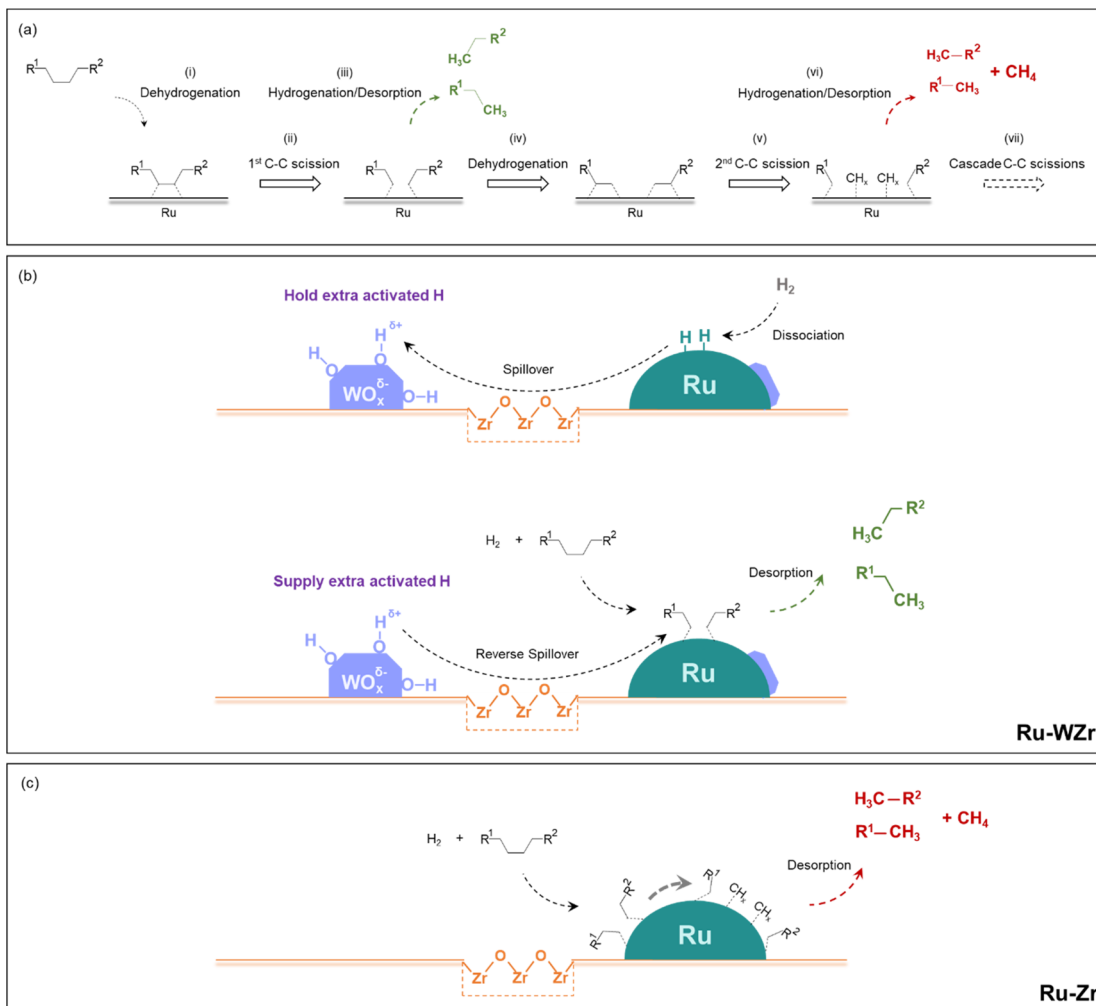
[a]a, Proposed reaction mechanism of LDPE hydrogenolysis on Ru-based catalysts. R^1, $R^2 = C_nH_{2n+1}$ ($n \geq 0$) alkyl groups. b, Selective pathway on Ru-WZr catalysts induced by ~1 nm, slightly reduced $(WO_x)_n$ clusters. c, Non-selective pathway on Ru-Zr in the absence of WO_x. The proximity of Ru and WO_x is not depicted exactly as WO_x covers some of the Ru. The reverse spillover mechanism is meant to include also other aspects, such as interfacial sites and a change in polymer−surface interactions.

that the Ru-catalyzed C−C bond activation, which is rate-limiting at high pressures, is not modified by WO_x incorporation. This is consistent with the n-hexane model reaction results (Figure S7c), which show an identical TOF per C−C bond scission over Ru-Zr and the two Ru-WZr catalysts (see detailed discussion in Supporting Information). Our structural characterizations show little difference in particle size of Ru-Zr and Ru-15WZr catalysts (see EXAFS results in Table S4), and XPS data also provide no evidence of electronic modification of Ru by WO_x. These findings altogether indicate that the contribution of Ru is not impacted by the WO_x incorporation. The benefit of Ru-WZr catalysts in H_2 deficient environments may arise from additional hydrogen, polymer−surface interaction, and/or interfacial sites created on these catalysts. The data suggests that the $(WO_x)_n$ clusters may supply extra H via reverse-spillover to facilitate the rate-limiting hydrogenation/desorption (iii) on the Ru surface or the interface or modify the polymer−catalyst interactions, enhancing both activity and selectivity and effectively changing the mechanism from Scheme 1c to Scheme 1b. We elaborate on this point next.

Role of Hydrogen on Ru-WZr Catalysts

TPR-MS and H_2-TPD-MS measurements provide further insights into the enhanced performance of Ru-15WZr. TPR-MS results (Figure 5a) show that, at low temperatures (300−600 K), Ru-Zr consumes roughly 0.6 mmol H_2/g, primarily due to the reduction of surface Ru oxides and Ru-15WZr consumes an extra of 0.3 mmol H_2/g. This additional hydrogen likely remains on the catalyst at least until 600 K because the formation of H_2O below 600 K on both Ru-Zr and Ru-15WZr is quite similar (Figure S11). The reduction of WO_x on 15WZr consumes ~1.9 mmol H_2/g. It occurs at a much higher temperature of ~900 K than Ru-15WZr. On the latter, the WO_x reduction peak is much broader and starts at much lower temperatures of ~600 K. The lower reduction temperature of WO_x on Ru-15WZr stems from Ru's role. These results indicate a possible hydrogen spillover, where Ru dissociates H_2 and H diffuses over to the $(WO_x)_n$ clusters. This extra H on $(WO_x)_n$ can be readily available for hydrogenation reactions on metallic Ru by the reverse spillover mechanism.[51]

TPD-MS results (Figure 5b) show that H_2 desorbed from Ru-15WZr (0.16 mmol/g) is 3-fold that from Ru-Zr (0.05
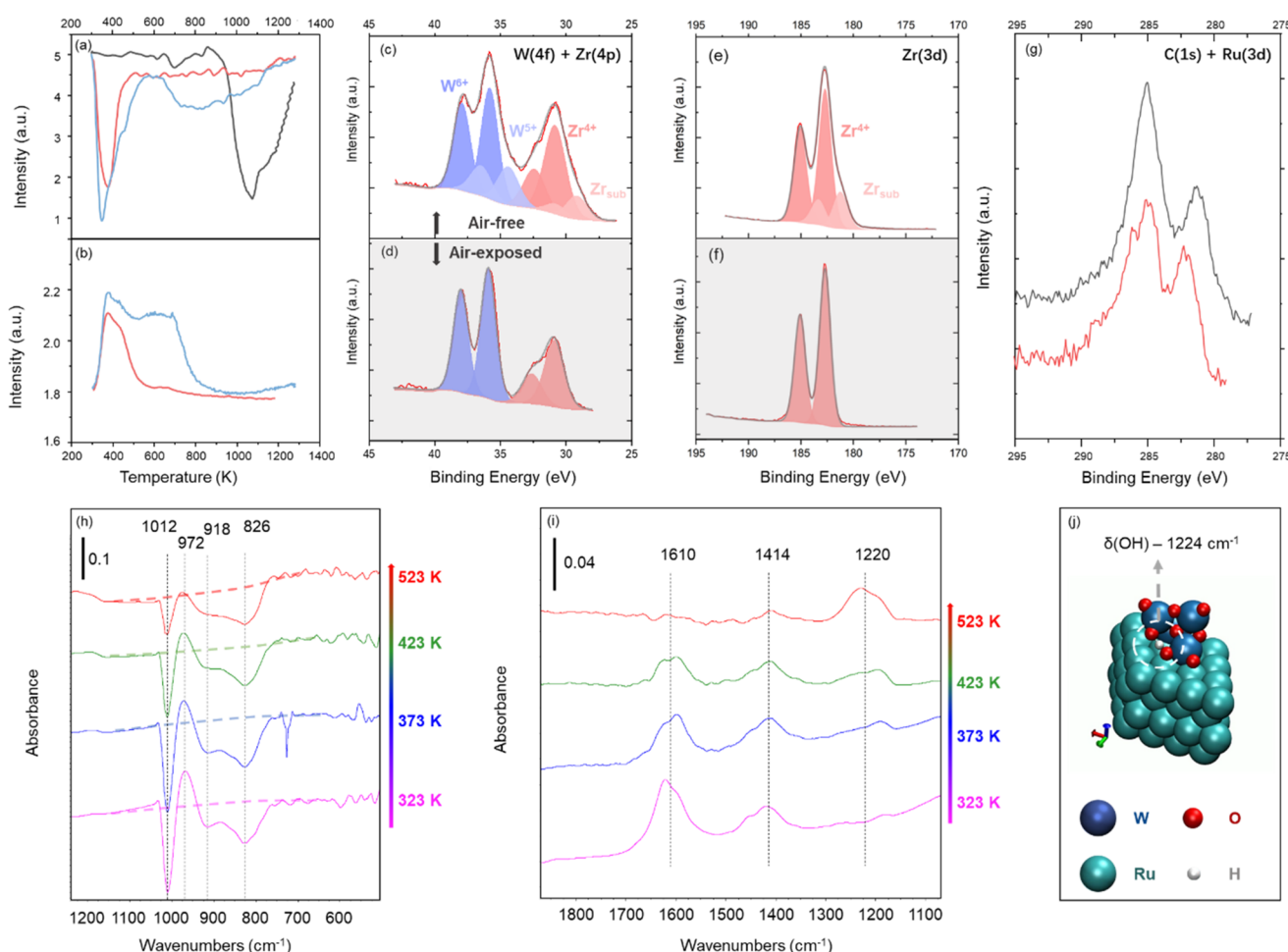
Figure 5. Role of hydrogen on Ru-15WZr catalyst. a, TPR-MS (negative features, m/z = 2). b, H_2-TPD-MS (positive features, m/z = 2) measurements on 15WZr (black), Ru-Zr (red), and Ru-15WZr (blue). c−f, XPS spectra of (c, e) air-free and (d, f) air-exposed Ru-15WZr catalyst in the (c, d) W 4f + Zr 4p region and (e, f) Zr 3d region. Contributions from W^{6+}, W^{5+}, Zr^{4+}, and partially reduced ZrO_2 were deconvoluted and are illustrated in purple, light purple, red, and light red, respectively. g, XPS spectra of air-free (black trace) and air-exposed (red trace) Ru-15WZr in the region of C 1s and Ru 3d for Ru metal, RuO_2, and/or $RuO_2 \cdot xH_2O$. All catalysts for XPS were pretreated in 10% H_2/He at 523 K for 1 h with the air-exposed samples being equilibrated in air at room temperature and the air-free samples being immediately transferred (at room temperature) for measurements without exposing to air (P_{O2} < 1000 ppm) using a vacuum transfer vessel. h and i, Difference IR spectra of Ru-15WZr at (pink) 323 K, (blue) 373 K, (green) 423 K, and (red) 523 K collected upon exposure to steady-state 10% H_2 flow carried by 60 sccm He. h, Stretching vibration regime of W═O and W−O−W groups. i, Bending vibration regime of O−H groups. Difference spectra were obtained by subtracting the absorbance spectra collected prior to H_2 exposure from the spectra post-H_2 exposure at each temperature. Horizontal dashed lines represent estimated baselines. j, Simulated bending vibration modes of hydroxyl on a W_4O_{12} cluster, supported on Ru(0001).

mmol/g), with a higher H binding energy, based on the desorption temperatures that extend beyond those of Ru-Zr and up to 800 K. DFT calculations (Table S6) of a W_4O_{12} cluster on Ru (0001), chosen as a model structure, confirms that the surface H on W−OH groups is bound significantly more strongly ($E_{binding}$ = −1.43, −1.29, and −1.05 eV) than on the Ru sites ($E_{binding}$ = −0.93, −0.82, and −0.44 eV). In contrast, a Ru-20WSi catalyst does not possess synergistic features in TPR and TPD measurements (Figure S12); at the same time, it lacks highly dispersed $(WO_x)_n$ clusters (XRD and Raman, Figure S13) and does not suppress methane formation (Figure S14).

Air-free XPS spectra in the W 4f + Zr 4p region (Figure 5c) and Zr 3d region (Figure 5e) were collected after pretreating Ru-15WZr at 523 K and 1 bar in a 10% H_2 flow. Deconvoluted and benchmarked spectra against the air-equilibrated ones are shown in Figure 5d,f. Both the air-exposed W and Zr oxides are at the highest valence, evidenced by doublets for W 4f at 38.0

and 36.0 eV, Zr 4p at 32.5 and 30.9 eV (Figure 5d), and Zr 3d at 185.0 and 182.7 eV (Figure 5f). Air-free Ru-15WZr (Figure 5c) shows reduction bands associated with both W^{5+} cations[52] (36.4 and 34.4 eV) and Zr suboxides (30.7 and 29.1 eV for Zr 4p and 183.4 and 181.2 eV for Zr 3d). Deconvolution of the W^{4+} center is impossible due to overlap with the Zr 4p and is omitted from the analysis. Since $(WO_x)_n$ clusters are predominantly ∼1 nm in size (within photoelectron escape depth), we estimate that roughly 30% of W^{6+} centers are reduced to 5+ (or lower) oxidation state based on the deconvolution area ratios.

Since little water forms from WO_x reduction up to 600 K, based on the TPR-MS on Ru-15WZr (Figure S11), we envision that hydrogen spillover leads to $H^{\delta+}$ interacting with the Lewis basic oxygen atoms (W═O or W−O−W) while injecting electrons into the W^{6+} centers to lower their oxidation state (Scheme 1b), similar to frustrated Lewis pairs.[53,54] Since the degree of hydrogen incorporation is in part

determined by the ability to delocalize the injected electrons into the conjugated base,[43] i.e., the $(WO_x)_n$ clusters, it is not surprising then that the hydrogen storage capacity is associated with the ~1 nm $(WO_x)_n$ clusters on Ru-15WZr rather than bulk crystallites on Ru-20WSi. The slight reduction of the ZrO_2 surface may also result from hydrogen spillover.[55] Since Ru and WO_x species are highly dispersed on ZrO_2 (Figure 3), the partially reduced ZrO_2 sites may be implicated by bridging $H^{\delta+}$ species and electrons between Ru and $(WO_x)_n$ islands (Scheme 1b). Such an effect is impossible on nonsemiconducting supports, such as SiO_2 (Scheme S1).

XPS bands associated with Ru 3d (Figure 5g) are complicated due to C 1s overlaps and interference between the Ru metal and hydrated/dehydrated oxides.[56] By subtracting the two Ru-15WZr spectra with and without air exposure, contributions of the metallic Ru $3d_{5/2}$ band (~280 eV) become evident in the air-free sample; yet, Ru is likely to remain slightly oxidized in the air-free sample, judging by the bandwidth and according to the literature on Ru/TiO_2.[57]

We performed *in situ* transmission FTIR measurements on Ru-15WZr catalyst under relevant reaction conditions (323–523 K and 1 bar in 10% H_2/He flow) and obtained difference absorbance spectra by subtracting the collected spectra before and after steady-state H_2 exposure at each temperature (see Figure S15 for spectra overview and peak assignments). All samples were pretreated in H_2 and purged in He at 623 K to ensure water formation does not interfere with the results acquired at lower temperatures.

Upon H_2 exposure, the difference IR features from 323 to 523 K in the W/O stretching regime (Figure 5h) are similar to a decrease in the dehydrated $\nu(W=O)$ mode[58] (1012 cm^{-1}) and an increase in the hydrated $\nu(W=O)$ mode[58] (972 cm^{-1}). Since pretreatments rule out water formation, we assign this band shift to W=O hydrogen bonding with the proximal $H^{\delta+}$ species and/or OH groups (i.e., W=O⋯H and/or W=O⋯H−O−W). The relative intensity of hydrated (+)/dehydrated (−) $\nu(W=O)$ bands decreases at higher temperatures, suggesting consumption of the W=O bonds at high temperatures and probable transformation into W−OH species with formal O−H bonds. The broad spectral envelope at 918 and 826 cm^{-1} can have contributions from both $\nu(W−O−Zr)$ and $\nu(W−O−W)$ modes,[59] as in the multiwavelength Raman approach on transitional metal oxides.[60] The decrease in the difference absorbance (Figure 5h) is possibly due to electron delocalization on $WO_x^{\delta-}$ species induced by charge separation of spillover hydrogen. Similar trends in the overtone regime at ~2000 cm^{-1} further corroborate the above changes (Figure S16). The same methodology on a benchmark 15WZr sample shows 1−2 orders of magnitude weaker changes in difference spectra (Figure S17) when the intensities of absolute absorbance spectra are comparable (Figure S18a,b). Moreover, the relative band areas of hydrated (+)/dehydrated (−) W=O features do not change significantly at elevated temperatures, suggesting that no W=O/W−OH transformations occur without hydrogen spillover from Ru. Difference features associated with $\nu(W−O−Zr)$ and $\nu(W−O−W)$ modes are absent, suggesting no charge separation on the $(WO_x)_n$ clusters without Ru. The W/O vibrational changes in response to H_2 exposure on both Ru-15WZr and 15WZr catalysts were subsequently confirmed by *in situ* Raman measurements (Figure S18c−f) performed under the same conditions.

Consistent difference absorbance for the $\delta(OH)$ modes on Ru-15WZr is depicted in Figure 5i. The corresponding $\nu(OH)$ modes exhibit very broad features at ~3000 cm^{-1} due to H-bonding and are shown in Figure S16b. In the $\delta(OH)$ regime, the band at ~1610 cm^{-1} resembles the deformation vibrations of water hydroxyls. In the absence of molecular water (Figure S19), we ascribe this feature to water-like surface species[61] that release molecular H_2, instead of H_2O, upon heating or evacuation. The difference features at ~1414 and 1200 cm^{-1} were previously assigned to $\delta(OH)$ modes of W−OH interaction with surface oxygen atoms to a different degree.[62−64] The band at 1610 cm^{-1} diminishes at elevated temperatures due to thermal instability.[37] The 1414 cm^{-1} feature remains stable and is ultimately reduced at 523 K. At high temperatures, a third, quite unusual $\delta(OH)$ band emerges at ~1220 cm^{-1}. DFT calculations of a W_4O_{12} cluster on Ru (0001), as a model structure (Figure 5j), reveal that this unique $\delta(OH)$ mode may be assigned to W−OH groups adjacent to a W=O group (Movie 1; details in Supporting Information). This bending vibration is absent in W_4O_{12} without Ru (Movie 2). We observed the ~1220 cm^{-1} band grows with increasing temperature, whereas the 1600 and 1414 cm^{-1} bands decrease in unison (Figure 5i). This is consistent with the decrease in the relative band areas of hydrated (+)/dehydrated (−) $\nu(W=O)$ features (Figure 5h), which suggest the transformation from W=O to W−O−H bonds. Experiments on 15WZr or Ru-Zr (Figure S19) hardly give any such difference features, highlighting the Ru-WO_x synergy in Ru-WZr. The $\delta(OH)$ bands at ~1610, 1414, and 1220 cm^{-1} were definitively assigned by replicating experiments using molecular deuterium (Figure S20). The observed $\delta(OD)$ wavenumbers agree well with those derived from the corresponding $\delta(OH)$ modes calculated using reduced mass. Relaxation of the H_2-equilibrated Ru-15WZr catalyst (Figure S21) shows that all the different features associated with $\nu(W/O)$ and $\delta(OH)$ modes nearly reversed to the original states when H_2 was removed from the feed stream at 523 K. This suggests that the extra H stored in hydroxyls is highly mobile, can reverse spillover back to the Ru surface, and may be subject to recombinative desorption of molecular H_2 (TPD, Figure 5b).

Collectively, multiple characterization approaches and DFT calculations corroborate the presence of an extra amount of highly mobile and active H species on the Ru-WZr catalysts. These H species can undergo reversible spillover between Ru and $(WO_x)_n$ clusters, aiding hydrogenation and desorption (iii, Scheme 1b), enhancing activity and selectivity in LDPE hydrogenolysis under H_2 deficient conditions. The correlation of H storage with selectivity is unambiguous. However, direct proof of the implication of the reverse spillover mechanism is not possible at this moment. We hypothesize that new interfacial sites created by OH and modified polymer−catalyst interactions could also possibly be at play. Further work is needed to dissect the precise mechanism.

■ DISCUSSION

We demonstrated that Ru-WZr catalysts are highly active and selective for LDPE hydrogenolysis at mild conditions (low temperatures, short times, a low catalyst to polymer mass ratio). Importantly, this performance extends to real-world plastic consumables, such as LDPE bottles, cling wraps, and pipettes, where reaction times could be shorter and conversions higher. Excitingly, they significantly suppress low-value methane formation and produce higher molecular weight fuels and wax/lubricant base-oils compared to Ru/C

and Ru/zeolites. They are also superior to Ru-Zr and Ru-WSi catalysts, demonstrating the WO_x and ZrO_2 support's profound role. The WO_x addition leverages Ru's high hydrogenolysis activity while overcoming its extensive chain cracking to methane. Characterization and DFT calculations confirm that the highly dispersed $(WO_x)_n$ clusters store H in surface hydroxyls by the spillover of H from the Ru active phase that dissociates molecular H_2. WO_x increases the catalyst hydrogen storage capacity essential for hydrogenating long-chain alkyl intermediates through reverse spillover to Ru or by creating new interfacial sites and/or modifying the catalyst–polymer interactions, leading to their desorption before they get overcracked. This novel mechanism of hydrogen storage overcomes significant compression costs associated with high H_2 pressures and opens up possibilities for materials design to further engineer plastics recycling.

■ MATERIALS AND METHODS

Preparation of Ru-WZ Catalysts

Ruthenium supported on tungstated zirconia (Ru-WZr) was synthesized using the successive incipient wetness impregnation method. The tungstated zirconia (WZr) support was prepared by impregnation of zirconium oxyhydroxide $(ZrO_x(OH)_{4-2x})$ with a solution of ammonium metatungstate hydrate $((NH_4)_6H_2W_{12}O_{40}\cdot xH_2O$, Aldrich, 99.99%). $ZrO_x(OH)_{4-2x}$ was made by hydrolysis of a zirconyl chloride octahydrate $(ZrOCl_2\cdot8H_2O$, Aldrich, 98%) solution using ammonium hydroxide $(NH_4OH$, Aldrich, 28–30 wt % in $H_2O)$. Both solutions were added dropwise in stirred water at pH of 10. The suspension was aged under vigorous stirring for 12 h, followed by alternating filtration and rinsing steps until Cl^- ions were no longer detectable in the filtrate. $ZrO_x(OH)_{4-2x}$ was dried at 383 K in static air for 12 h and then impregnated with the $(NH_4)_6H_2W_{12}O_{40}\cdot xH_2O$ solution, followed by drying at 383 K for 12 h and calcination in static air at 1073 K for 3 h (2 K/min ramp). WZr supports loaded with 15 and 25 wt % WO_3 are denoted as 15WZr and 25WZr. The as-prepared WZr support was subsequently impregnated with a calculated amount of ruthenium(III) nitrosyl nitrate solution $(Ru(NO)(NO_3)_x(OH)_{3-x}$, Aldrich, 1.5 wt % Ru) to achieve 5 wt % nominal metal loading. The resulting slurry was dried at 383 K for 12 h and then subjected to a 2 h reduction treatment, carried out in a tubular reactor using 10% H_2 in a 100 sccm He carrier gas at 523 K. The control catalysts, Ru supported on bare zirconia, tungstated silica, ceria, HY zeolite, and [Al]MCM-41 material (Ru-Zr, Ru-WSi, Ru-Ce, Ru-HY, and Ru-[Al]MCM-41), were prepared by the same Ru impregnation procedure. Zirconia was prepared by calcining $ZrO_x(OH)_{4-2x}$ in air at 823 K for 3 h, WSi was prepared by the same procedure as WZr except for using amorphous fumed silica (175–225 m^2/g, Alfa Aesar). Ceria (Sigma-Aldrich, Product No.: 700290), HY (Si/Al$_2$ = 30, Zeolyst), and [Al]MCM-41(Si/Al$_2$ = 25, ACS Material) were pretreated at 723 K in air for 2 h prior to Ru impregnation. A 5 wt % Ru on carbon catalyst (Ru-C, Sigma-Aldrich, 206180) was directly purchased from the vendor. Since all catalysts used in this study have the same 5 wt % Ru nominal loading, this value of 5% is omitted throughout the main text.

Reactivity Studies for LDPE Hydrogenolysis

Prior to the reactivity measurements, all catalysts were prereduced *ex situ* in a continuous follow reactor at 523 K for 1 h (10 K/min ramping rate) using 10% H_2 in 100 sccm He flow. The catalysts were cooled down to room temperature, briefly exposed to air, and mixed with 2 g of low-density polyethylene ($M_w \sim$ 76 kDa, Sigma-Aldrich, Product No. 428043) using a typical LDPE-to-catalyst mass ratio of 40. The mixture was then transferred into a 50 mL stainless-steel Parr reactor together with a 700 μL stir bar. The sealed reactor was purged five times with H_2 at 30 bar and then charged to 30 bar (standard temperature and pressure, STP) for the reaction. The reactor was quickly heated up to 523 K in 20 min, maintained at 523 K for 2 h

under stirring at 500 rpm (free of external H_2 diffusion limitation; higher stirring rates did not change the reactivity), and then quenched in a water−ice bath to below 283 K for product collection. Reaction reproducibility is verified using five independent batches of Ru-Zr and Ru-15WZr catalysts synthesized over 6 months (Figure S22). Hydrogenolysis of single-use LDPE bottles (H−B Instrument, Cat No.: 106260005), cling wraps (Clorox, Glad CLO00020), and pipettes (Fisher Scientific, Cat No. 13-711-7M) were performed following the same procedure. The substances were trimmed into ∼5 × 5 mm^2 pieces prior to mixing with the catalyst.

n-Hexane Hydrogenolysis

The steady-state reaction rates for *n*-hexane (Aldrich, ≥99%) hydrogenolysis were measured at 1 bar and 523 K in a continuous flow reactor that consisted of an 18-in. long, 1/4-in. ID quartz tube placed vertically in a tube furnace. The catalyst bed (typically 100 mg) was diluted 100 times using inert ZrO_2 supports and held in place by quartz-wool plugs and coarse quartz pellets loaded on both ends of the catalyst bed. The reactor was custom-made to insert a thermocouple, protected by a quartz protection sleeve, at the center of the catalyst bed. Before the kinetic measurements, the catalyst was pretreated at 523 K (10 K/min ramping rate) for 1 h in 10% H_2 in 100 sccm He. *n*-Hexane (1−2%) was injected into a He carrier flow using a syringe pump (New Era Pump System) and mixed with H_2 flow before entering the reactor.

Product Analysis

Products from the probe reaction of *n*-hexane hydrogenolysis were analyzed online using an FID gas chromatography equipped with an Agilent HP-Plot GC column. For the LDPE hydrogenolysis reactions, *gaseous products*, typically C1−C6, from the Parr reactor headspace were sampled at 283 K using a 1 L Tedlar bag and analyzed using the aforementioned GC. Quantification was done using standard calibration mixtures. Hydrocarbon products, typically C4−C35, were extracted from the liquid−solid residuals using a 20 mL of dichloromethane (CH_2Cl_2, Fisher Scientific, ACS grade) solution with 20 mg of *n*-octacosane (external standard, *n*-C28, TCI chemicals, >98%). Since the reaction produces a small amount of *n*-C28, the signal of internal standard is calculated from the raw *n*-C28 signal minus the estimated *n*-C28 product signal using an average of *n*-C27 and *n*-C29. The *soluble products* were analyzed using GC-MS (Agilent, DB-1 column) for identification and GC-FID (Agilent HP-1 column) for quantification. A representative raw GC trace is shown in Figure S23. Calibration of GC signals was conducted using normal alkanes standard mixtures, and alkane isomers were assumed to have the same calibration factor as the corresponding normal alkanes. The catalyst and remaining solids were filtered, dried in air for 24 h, and weighed prior to further characterization.

The yield of product alkanes with *i* carbons (C_i) was calculated using the following equation:

$$Y_i = \frac{n_i}{n_{initial}}$$

where n_i is the moles of carbon in C_i, and $n_{initial}$ is the same in the initial LDPE feedstock. The selectivity of product alkanes with *i* carbons (C_i) is evaluated from

$$S_i = \frac{Y_i}{\sum_{non\text{-}solid} Y_i}$$

Here $\sum_{nonsolid} Y_i$ corresponds to the yield of nonsolid products—namely, the combined yield of all *gaseous* and *soluble* liquid products.

High-resolution differential scanning calorimetry (DSC, Discovery, TA Instruments) measurements were performed to characterize the melting temperature and heat of fusion for pristine LDPE and the solid residues collected after filtration.

Catalyst Characterization

X-ray diffraction (XRD) patterns of powdered materials were measured using a Bruker D8 diffractometer equipped with a Cu Kα source. The BET surface area and porosity were measured using N_2 as

the adsorbent at 77 K with a Micromeritics ASAP 2020 instrument. Raman spectra were obtained with a LabRAM high-resolution Raman spectrometer (HORIBA) equipped with a He−Cd excitation UV laser with a wavelength of 325 nm and a green line solid-state laser with a wavelength of 532 nm. *In situ* Raman spectroscopy was performed in an environmentally controlled high-temperature cell (Harrick). Elemental analysis was carried out on a wavelength-dispersive X-ray fluorescence spectrometer (WDXRF, Rigaku, Supermini 200) equipped with a high-powered (200 W) X-ray tube. For X-ray photoelectron spectroscopy (XPS) analysis, powdered samples were pressed onto Cu foils. XPS spectra were collected using a Thermo Fisher K-Alpha Instrument equipped with an Al(K) X-ray source. Samples used in air-free XPS measurements were pretreated in a tubular flow reactor using 10% H_2 in a 100 sccm He carrier gas for 2 h at 523 K. The cooled reactor was then sealed and moved into a glovebox ($P_{O_2} < 1000$ ppm), where the samples were transferred into a designated vacuum vessel for XPS measurements. Selected results of compositional and geometrical characterizations described above are summarized in Table S2.

Bright-field transmission electron microscopy (BF-TEM) was performed with a field emission gun transmission electron microscope (JEOL, JEM-2010F), operated at an accelerating voltage of 200 kV. Dark-field scanning transmission electron microscopy was performed with a JEOL NEOARM operating at 200 kV. The samples were diluted in isopropanol and deposited on a lacey carbon film on copper grids provided by Electron Microscopy Sciences. The probe current was 120 pA with a condenser lens aperture of 40 μm and a camera length of 4 cm. Energy-dispersive X-ray spectroscopy was performed with the same parameters, with the exception of a camera length of 2 cm. Two silicon drift detectors (SDD) provided by JEOL were used, and the maps were obtained with DigitalMicrograph, a software provided by Gatan Inc.

Apparent dispersions of Ru were measured on a Micromeritics AutoChem II instrument following a customized procedure of H_2 chemisorption reported by Iglesia and coworkers.[65] This method has previously been shown to have an $H_2/Ru = 1$ stoichiometry and is not affected by the reduction history of Ru or SMSI effect. In brief, the sample was pretreated *in situ* under 10% H_2/Ar flow for 1 h at 523 K followed by purging in pure Ar flow for 1 h at 523 K. The sample was cooled under Ar, maintained at 200 K (±10 K) using a liquid N_2−ethanol bath, and subsequently treated in a 1% O_2/He mixture at 200 K for 15 min followed by purging in Ar flow at 200 K for 15 min. Finally, the sample was heated in Ar flow and maintained at 373 K for 1 h. Ru dispersions were measured using pulse H_2 chemisorption at 373 K. Results from all catalysts used in this study are tabulated in Table S3. Conventional chemisorption of neither H_2 nor CO using simple pulse techniques at room temperature is reliable (Table S7). This is in part due to the activation energy of H_2 adsorption on Ru at room temperature,[66] especially on catalysts that featured fairly strong metal−support interaction (underestimation of Ru dispersion) and the fast reaction activation of CO on the Ru surface (overestimation of Ru dispersion).

Temperature-programmed reduction (TPR) and temperature-programmed desorption (TPD) of adsorbed hydrogen (H_2-TPD) were carried out in combination with mass spectroscopy (MS) analysis (Pfeiffer Vacuum Ominstar GSD 301C quadrupole mass spectrometer) using a continuous flow reactor. For TPR-MS measurements, the sample was purged in He at 523 K for 1 h and cooled down to room temperature in He flow. A 60 sccm, 5% H_2 in He flow was stabilized to steady state for at least 1 h. The TPR measurement was then carried out at a ramping rate of 10 K/min from 300 to 1273 K. For H_2-TPD analysis, the sample was prereduced in a 60-sccm, 5% H_2 in He mixed flow at 523 K for 1 h, cooled down to room temperature, and purged in a 60-sccm He flow for at least 1 h to stabilize the baseline of the H_2 MS. The H_2-TPD measurement was then carried out using the same ramping procedure as H_2-TPD. MS signals were calibrated using a MicroGC (990 MicroGC, Agilent) equipped with an MS5A column. The MS signal for He was used as an internal reference for semiquantification of H_2 uptake/desorption.

FTIR transmission spectra were acquired on a Nicolet 8700 spectrometer (Thermo Scientific) equipped with a liquid nitrogen cooled MCT detector and a custom-made Pyrex *in situ* flow cell sealed with KBr windows on both ends. Powdered samples were pressed into a self-supported disk (~12.5 mg, 1000 PSI) and aligned with the laser path using a quartz holder. FTIR measurements were performed to analyze the hydrogen surface species at temperatures ranging from 323 to 523 K. Moisture was removed from the gas feed by a liquid nitrogen trap. In order to eliminate the interferences from bulk reduction or water formation, all samples were prereduced *in situ* at 623 K for 1 h in 10% H_2 carried by 60 sccm He flow and then purged in pure He at 623 K for 1 h to remove adsorbed hydrogen. Difference spectra were obtained at 323, 373, 423, and 523 K by subtracting each reference spectrum collected in He from the steady-state spectrum taken in H_2 in He flow at the same temperature. Experiments with deuterium gas (D_2, Cambridge Isotope Laboratories, D-99.8%) with the same methodology were repeated in order to confirm the hydroxyl vibration modes.

FTIR of adsorbed pyridine was also performed to characterize the Brønsted and Lewis acid sites. The sample was pretreated in He flow at 523 for 1 h and then cooled and maintained at 423 K. The sample was then saturated by pyridine vapor introduced by passing He flow through a bubbler filled with liquid pyridine (Aldrich, 99.8%). Prior to spectrum acquisition, the sample was purged with pure He flow for 30 min to desorb weakly bonded pyridine thermally.

X-ray absorption spectroscopy (XAS) data were collected for the Ru K-edge (22.117 keV) at the QAS 7-BM beamline of NSLS-II at Brookhaven National Laboratory. The spectra of the reference (Ru foil) were measured in transmission mode, while spectra of sample catalysts were recorded in fluorescence mode. Before measurements, the sample was packed in a quartz tube connected to a gas line. Then the catalyst was reduced in 20 mL/min flow of a 50% H_2/He mixture at 473 K for 30 min. Spectra were collected after reduction. Spectra were subjected to standard data processing using Athena and Artemis software.[67]

Modeling

Density functional theory calculations (DFT) were performed by the plane-wave based Vienna ab initio simulation package (VASP), version 5.4.4.[68−70] The electron−electron exchange and correlation energies were computed using the Perdew, Burke, and Ernzerhof functionals with D3 dispersion corrections developed by Grimme.[71,72] Core electrons were treated with the projector augmented-wave (PAW) pseudopotentials.[68,73] The Ru (0001) surface was simulated using a four-layer 4×4 unit cell. The lattice constant of Ru was calculated to be 2.725 Å, in close agreement with the experimental value of 2.71 Å.[74] The supported WO_3 (0001) tetramer was constructed by cleaving a $2 \times 1 \times 1$ unit cell from the monoclinic bulk WO_3, which features lattice parameters of $a = 5.358$, $b = 5.413$, and $c = 7.722$ Å. The lattice parameters are in good agreement with experimental values of $a = 5.28$, $b = 5.16$, and $c = 7.66$ Å.[75] The bottom two layers of Ru were held fixed during calculations, whereas the rest of all the atoms were allowed to relax. A vacuum padding between the slabs was set at a height of 16.5 Å to minimize the interaction in the *z*-direction. In addition, dipole corrections were applied normal to the surface. The Brillouin zone was integrated using a $3 \times 3 \times 1$ k-mesh based on the Monkhorst−Pack method,[76] with Gaussian smearing of 0.1 eV. For the plane-wave set, a cutoff energy of 400 eV was used. Electronic structure calculations were performed iteratively, and electronic structures were converged when the difference in energy between subsequent steps fell below 10^{-6} eV. Geometries of adsorbate−metal systems were optimized until the maximum of all forces fell below 0.02 eV/Å. Vibrational modes analysis was carried out using the central finite difference method. In these calculations, atoms were displaced by 0.05 Å in all directions by the VASP default. In the vibrational mode calculations, the adsorbate-hydrogen and the WO_3 cluster were displaced.

■ AUTHOR INFORMATION

Corresponding Author

Dionisios G. Vlachos − *Center for Plastics Innovation, University of Delaware, Newark, Delaware 19716, United States; Department of Chemical and Biomolecular Engineering, University of Delaware, Newark, Delaware 19716, United States;* ⓞ orcid.org/0000-0002-6795-8403; Email: vlachos@udel.edu

Authors

Cong Wang − *Center for Plastics Innovation, University of Delaware, Newark, Delaware 19716, United States;* ⓞ orcid.org/0000-0002-0451-344X

Tianjun Xie − *Center for Plastics Innovation, University of Delaware, Newark, Delaware 19716, United States*

Pavel A. Kots − *Center for Plastics Innovation, University of Delaware, Newark, Delaware 19716, United States*

Brandon C. Vance − *Center for Plastics Innovation, University of Delaware, Newark, Delaware 19716, United States; Department of Chemical and Biomolecular Engineering, University of Delaware, Newark, Delaware 19716, United States*

Kewei Yu − *Department of Chemical and Biomolecular Engineering, University of Delaware, Newark, Delaware 19716, United States*

Pawan Kumar − *Department of Materials Science and Engineering, University of Pennsylvania, Philadelphia, Pennsylvania 19104, United States;* ⓞ orcid.org/0000-0002-5764-2915

Jiayi Fu − *Department of Chemical and Biomolecular Engineering, University of Delaware, Newark, Delaware 19716, United States*

Sibao Liu − *Key Laboratory for Green Chemical Technology of Ministry of Education, School of Chemical Engineering and Technology, Tianjin University, Tianjin 300072, China*

George Tsilomelekis − *Department of Chemical and Biochemical Engineering, School of Engineering, Rutgers, The State University of New Jersey, Piscataway, New Jersey 08854, United States;* ⓞ orcid.org/0000-0002-0435-8216

Eric A. Stach − *Department of Materials Science and Engineering, University of Pennsylvania, Philadelphia, Pennsylvania 19104, United States;* ⓞ orcid.org/0000-0002-3366-2153

Weiqing Zheng − *Center for Plastics Innovation, University of Delaware, Newark, Delaware 19716, United States*

Complete contact information is available at:
https://pubs.acs.org/10.1021/jacsau.1c00200

■ REFERENCES

(1) Giacovelli, C. *Single-Use Plastics: A Roadmap for Sustainability*; UNEP: 2018; revised edition, pp vi; 6.

(2) OECD. *Improving Plastics Management: Trends, policy responses, and the role of international co-operation and trade*; Environmental Policy Paper No. 12; 2018.

(3) Geyer, R.; Jambeck, J. R.; Law, K. L. Production, use, and fate of all plastics ever made. *Science Advances* **2017**, *3* (7), No. e1700782.

(4) U.S. Environmental Protection Agency. *Advancing Sustainable Materials Management: Facts and Figures Report*; 2020.

(5) Goldman, A. S. Catalytic Alkane Metathesis by Tandem Alkane Dehydrogenation-Olefin Metathesis. *Science* **2006**, *312* (5771), 257−261.

(6) Ellis, L. D.; Orski, S. V.; Kenlaw, G. A.; Norman, A. G.; Beers, K. L.; Román-Leshkov, Y.; Beckham, G. T. Tandem Heterogeneous Catalysis for Polyethylene Depolymerization via an Olefin-Intermediate Process. *ACS Sustainable Chem. Eng.* **2021**, *9* (2), 623−628.

(7) Bäckström, E.; Odelius, K.; Hakkarainen, M. Trash to Treasure: Microwave-Assisted Conversion of Polyethylene to Functional Chemicals. *Ind. Eng. Chem. Res.* **2017**, *56* (50), 14814−14821.

(8) Celik, G.; Kennedy, R. M.; Hackler, R. A.; Ferrandon, M.; Tennakoon, A.; Patnaik, S.; LaPointe, A. M.; Ammal, S. C.; Heyden, A.; Perras, F. A.; et al. Upcycling Single-Use Polyethylene into High-Quality Liquid Products. *ACS Cent. Sci.* **2019**, *5* (11), 1795−1803.

(9) Serrano, D. P.; Aguado, J.; Escola, J. M. Developing Advanced Catalysts for the Conversion of Polyolefinic Waste Plastics into Fuels and Chemicals. *ACS Catal.* **2012**, *2* (9), 1924−1941.

(10) Mark, L. O.; Cendejas, M. C.; Hermans, I. The Use of Heterogeneous Catalysis in the Chemical Valorization of Plastic Waste. *ChemSusChem* **2020**, *13* (22), 5808−5836.

(11) Sharratt, P. N.; Lin, Y.-H.; Garforth, A. A.; Dwyer, J. Investigation of the Catalytic Pyrolysis of High-Density Polyethylene over a HZSM-5 Catalyst in a Laboratory Fluidized-Bed Reactor. *Ind. Eng. Chem. Res.* **1997**, *36* (12), 5118−5124.

(12) Vance, B. C.; Kots, P. A.; Wang, C.; Hinton, Z. R.; Quinn, C. M.; Epps, T. H.; Korley, L. T. J.; Vlachos, D. G. Single Pot Catalyst Strategy to Branched Products via Adhesive Isomerization and Hydrocracking of Polyethylene over Platinum Tungstated Zirconia. *Appl. Catal., B* **2021**, 120483.

(13) Zhao, D.; Wang, X.; Miller, J. B.; Huber, G. W. The Chemistry and Kinetics of Polyethylene Pyrolysis: A Process to Produce Fuels and Chemicals. *ChemSusChem* **2020**, *13* (7), 1764−1774.

(14) Munir, D.; Amer, H.; Aslam, R.; Bououdina, M.; Usman, M. R. Composite zeolite beta catalysts for catalytic hydrocracking of plastic waste to liquid fuels. *Materials for Renewable and Sustainable Energy* **2020**, *9* (2), 9.

(15) Aguado, J.; Sotelo, J. L.; Serrano, D. P.; Calles, J. A.; Escola, J. M. Catalytic Conversion of Polyolefins into Liquid Fuels over MCM-41: Comparison with ZSM-5 and Amorphous SiO2-Al2O3. *Energy Fuels* **1997**, *11* (6), 1225−1231.

(16) Aguado, J.; Serrano, D.; San Miguel, G.; Escola, J.; Rodríguez, J. Catalytic activity of zeolitic and mesostructured catalysts in the cracking of pure and waste polyolefins. *J. Anal. Appl. Pyrolysis* **2007**, *78* (1), 153−161.

(17) Chen, C. Y.; O'Rear, D. J.; Leung, P. Molecular Redistribution and Molecular Averaging: Disproportionation of Paraffins via Bifunctional Catalysis. *Top. Catal.* **2012**, *55* (19−20), 1344−1361.

(18) Pyra, K.; Tarach, K. A.; Śrębowata, A.; Melián-Cabrera, I.; Góra-Marek, K. Pd-modified beta zeolite for modulated hydro-cracking of low-density polyethylene into a paraffinic-rich hydro-carbon fuel. *Appl. Catal., B* **2020**, *277*, 119070.

(19) Liu, S.; Kots, P. A.; Vance, B. C.; Danielson, A.; Vlachos, D. G. Plastic waste to fuels by hydrocracking at mild conditions. *Science Advances* **2021**, *7* (17), No. eabf8283.

(20) Bin Jumah, A.; Tedstone, A. A.; Garforth, A. A. Hydrocracking of virgin and post-consumer polymers. *Microporous Mesoporous Mater.* **2021**, *315*, 110912.

(21) Bin Jumah, A.; Anbumuthu, V.; Tedstone, A. A.; Garforth, A. A. Catalyzing the Hydrocracking of Low Density Polyethylene. *Ind. Eng. Chem. Res.* **2019**, *58* (45), 20601−20609.

(22) Hesse, N. D.; White, R. L. Polyethylene catalytic hydrocracking by PtHZSM-5, PtHY, and PtHMCM-41. *J. Appl. Polym. Sci.* **2004**, *92* (2), 1293−1301.

(23) Nakaji, Y.; Tamura, M.; Miyaoka, S.; Kumagai, S.; Tanji, M.; Nakagawa, Y.; Yoshioka, T.; Tomishige, K. Low-Temperature Catalytic Upgrading of Waste Polyolefinic Plastics into Liquid Fuels and Waxes. *Appl. Catal., B* **2021**, *285*, 119805.

(24) Rorrer, J. E.; Beckham, G. T.; Román-Leshkov, Y. Conversion of Polyolefin Waste to Liquid Alkanes with Ru-Based Catalysts under Mild Conditions. *JACS Au* **2021**, *1* (1), 8−12.

(25) Zhang, F.; Zeng, M.; Yappert, R. D.; Sun, J.; Lee, Y.-H.; Lapointe, A. M.; Peters, B.; Abu-Omar, M. M.; Scott, S. L.

(26) Sánchez-Rivera, K. L.; Huber, G. W. Catalytic Hydrogenolysis of Polyolefins into Alkanes. *ACS Cent. Sci.* **2021**, *7* (1), 17−19.

(27) Tennakoon, A.; Wu, X.; Paterson, A. L.; Patnaik, S.; Pei, Y.; Lapointe, A. M.; Ammal, S. C.; Hackler, R. A.; Heyden, A.; Slowing, I. I.; Coates, G. W.; Delferro, M.; Peters, B.; Huang, W.; Sadow, A. D.; Perras, F. A. Catalytic upcycling of high-density polyethylene via a processive mechanism. *Nature Catalysis* **2020**, *3* (11), 893−901.

(28) Jia, C.; Xie, S.; Zhang, W.; Intan, N. N.; Sampath, J.; Pfaendtner, J.; Lin, H. Deconstruction of high-density polyethylene into liquid hydrocarbon fuels and lubricants by hydrogenolysis over Ru catalyst. *Chem. Catalysis* **2021**, *1*, 437.

(29) Lee, W.-T.; Bobbink, F. D.; Van Muyden, A. P.; Lin, K.-H.; Corminboeuf, C.; Zamani, R. R.; Dyson, P. J. Catalytic hydrocracking of synthetic polymers into grid-compatible gas streams. *Cell Reports Physical Science* **2021**, *2* (2), 100332.

(30) Yuan, C.; Emelianov, D. A.; Varfolomeev, M. A.; Pu, W.; Ushakova, A. S. Oxidation Behavior and Kinetics of Eight C20−C54 n-Alkanes by High Pressure Differential Scanning Calorimetry (HP-DSC). *Energy Fuels* **2018**, *32* (7), 7933−7942.

(31) Urabe, Y.; Takamizawa, K. The Determination of The Homologous Purity of Higher Normal Alkanes up to Dohectane with Capillary Gas Chromatography. *Polym. J.* **1994**, *26* (3), 283−289.

(32) Shen, L.; Severn, J.; Bastiaansen, C. W. M. Drawing behavior and mechanical properties of ultra-high molecular weight poly-ethylene blends with a linear polyethylene wax. *Polymer* **2018**, *153*, 354−361.

(33) Haynes, W. M. *CRC Handbook of Chemistry and Physics*; CRC Press: 2014.

(34) Luo, X.; Xie, S.; Liu, J.; Hu, H.; Jiang, J.; Huang, W.; Gao, H.; Zhou, D.; Lü, Z.; Yan, D. The relationship between the degree of branching and glass transition temperature of branched polyethylene: experiment and simulation. *Polym. Chem.* **2014**, *5* (4), 1305−1312.

(35) Marinkovic, N.; Sasaki, K.; Adzic, R. Nanoparticle size evaluation of catalysts by EXAFS: Advantages and limitations. *Zast. Mater.* **2016**, *57* (1), 101−109.

(36) Okazoe, S.; Kusada, K.; Wu, D.; Yamamoto, T.; Toriyama, T.; Matsumura, S.; Kawaguchi, S.; Kubota, Y.; Kitagawa, H. Synthesis of Mo and Ru solid-solution alloy NPs and their hydrogen evolution reaction activity. *Chem. Commun.* **2020**, *56* (92), 14475−14478.

(37) Solonin, Y. M.; Khyzhun, O. Y.; Graivoronskaya, E. A. Nonstoichiometric Tungsten Oxide Based on Hexagonal WO3. *Cryst. Growth Des.* **2001**, *1* (6), 473−477.

(38) Djaoued, Y.; Priya, S.; Balaji, S. Low temperature synthesis of nanocrystalline WO3 films by sol−gel process. *J. Non-Cryst. Solids* **2008**, *354* (2−9), 673−679.

(39) Zhou, W.; Ross-Medgaarden, E. I.; Knowles, W. V.; Wong, M. S.; Wachs, I. E.; Kiely, C. J. Identification of active Zr−WO x clusters on a ZrO 2 support for solid acid catalysts. *Nat. Chem.* **2009**, *1* (9), 722.

(40) Wang, C.; Lee, J. D.; Ji, Y.; Onn, T. M.; Luo, J.; Murray, C. B.; Gorte, R. J. A Study of Tetrahydrofurfuryl Alcohol to 1,5-Pentanediol Over Pt−WOx/C. *Catal. Lett.* **2018**, *148* (4), 1047−1054.

(41) Zhou, W.; Soultanidis, N.; Xu, H.; Wong, M. S.; Neurock, M.; Kiely, C. J.; Wachs, I. E. Nature of Catalytically Active Sites in the Supported WO3/ZrO2 Solid Acid System: A Current Perspective. *ACS Catal.* **2017**, *7* (3), 2181−2198.

(42) Wang, C.; Mao, X.; Lee, J.; Onn, T.; Yeh, Y.-H.; Murray, C.; Gorte, R. A Characterization Study of Reactive Sites in ALD-Synthesized WOx/ZrO2 Catalysts. *Catalysts* **2018**, *8* (7), 292.

(43) Iglesia, E.; Barton, D. G.; Soled, S. L.; Miseo, S.; Baumgartner, J. E.; Gates, W. E.; Fuentes, G. A.; Meitzner, G. D. Selective isomerization of alkanes on supported tungsten oxide acids. *Stud. Surf. Sci. Catal.* **1996**, *101*, 533−542.

(44) Flaherty, D. W.; Hibbitts, D. D.; Iglesia, E. Metal-Catalyzed C−C Bond Cleavage in Alkanes: Effects of Methyl Substitution on

Polyethylene upcycling to long-chain alkylaromatics by tandem hydrogenolysis/aromatization. *Science* **2020**, *370* (6515), 437−441.

Transition-State Structures and Stability. *J. Am. Chem. Soc.* **2014**, *136* (27), 9664−9676.

(45) Sinfelt, J. H. Catalytic hydrogenolysis on metals. *Catal. Lett.* **1991**, *9* (3−4), 159−171.

(46) Weisz, P. B. Polyfunctional heterogeneous catalysis. *Adv. Catal.* **1962**, *13*, 137−190.

(47) Wang, C.; Li, S.; Mao, X.; Caratzoulas, S.; Gorte, R. J. H-D Exchange of Simple Aromatics as a Measure of Brønsted-Acid Site Strengths in Solids. *Catal. Lett.* **2018**, *148* (11), 3548−3556.

(48) Carter, J.; Cusumano, J.; Sinfelt, J. Hydrogenolysis of n-heptane over unsupported metals. *J. Catal.* **1971**, *20* (2), 223−229.

(49) Oya, S.-I.; Kanno, D.; Watanabe, H.; Tamura, M.; Nakagawa, Y.; Tomishige, K. Catalytic Production of Branched Small Alkanes from Biohydrocarbons. *ChemSusChem* **2015**, *8* (15), 2472−2475.

(50) Nakagawa, Y.; Oya, S. i.; Kanno, D.; Nakaji, Y.; Tamura, M.; Tomishige, K. J. C. Regioselectivity and Reaction Mechanism of Ru-Catalyzed Hydrogenolysis of Squalane and Model Alkanes. *ChemSusChem* **2017**, *10* (1), 189−198.

(51) Prins, R. Hydrogen spillover. Facts and fiction. *Chem. Rev.* **2012**, *112* (5), 2714−2738.

(52) Wang, C.; Mironenko, A. V.; Raizada, A.; Chen, T.; Mao, X.; Padmanabhan, A.; Vlachos, D. G.; Gorte, R. J.; Vohs, J. M. J. A. C. Mechanistic study of the direct hydrodeoxygenation of m-cresol over WO x-decorated Pt/C catalysts. *ACS Catal.* **2018**, *8* (9), 7749−7759.

(53) Jia, J.; Qian, C.; Dong, Y.; Li, Y. F.; Wang, H.; Ghoussoub, M.; Butler, K. T.; Walsh, A.; Ozin, G. A. Heterogeneous catalytic hydrogenation of CO2 by metal oxides: defect engineering − perfecting imperfection. *Chem. Soc. Rev.* **2017**, *46* (15), 4631−4644.

(54) Zhao, X.; Wang, J.; Yang, M.; Lei, N.; Li, L.; Hou, B.; Miao, S.; Pan, X.; Wang, A.; Zhang, T. Selective Hydrogenolysis of Glycerol to 1,3-Propanediol: Manipulating the Frustrated Lewis Pairs by Introducing Gold to Pt/WOx. *ChemSusChem* **2017**, *10* (5), 819−824.

(55) Jung, K.-D.; Bell, A. T. Role of Hydrogen Spillover in Methanol Synthesis over Cu/ZrO2. *J. Catal.* **2000**, *193* (2), 207−223.

(56) Morgan, D. J. Resolving ruthenium: XPS studies of common ruthenium materials. *Surf. Interface Anal.* **2015**, *47* (11), 1072−1079.

(57) Coq, B.; Crabb, E.; Warawdekar, M.; Bond, G. C.; Slaa, J. C.; Galvagno, S.; Mercadante, L.; Ruiz, J. G.; Sanchez Sierra, M. C. Catalytic and structural properties of ruthenium bimetallic catalysts: Preparation and characterization. *J. Mol. Catal.* **1994**, *92* (1), 107−121.

(58) Ross-Medgaarden, E. I.; Wachs, I. E. Structural determination of bulk and surface tungsten oxides with UV- vis diffuse reflectance spectroscopy and raman spectroscopy. *J. Phys. Chem. C* **2007**, *111* (41), 15089−15099.

(59) Rossmedgarden, E.; Knowles, W.; Kim, T.; Wong, M.; Zhou, W.; Kiely, C.; Wachs, I. New insights into the nature of the acidic catalytic active sites present in ZrO2-supported tungsten oxide catalysts. *J. Catal.* **2008**, *256* (1), 108−125.

(60) Drake, T. L.; Stair, P. C. Multiwavelength Raman Spectroscopic Characterization of Alumina-Supported Molybdenum Oxide Prepared by Vapor Deposition. *Top. Catal.* **2017**, *60* (19−20), 1618−1630.

(61) Ishikawa, H.; Kondo, J. N.; Domen, K. Hydrogen adsorption on Ru/ZrO2 studied by FT-IR. *J. Phys. Chem. B* **1999**, *103* (16), 3229−3234.

(62) Daniel, M. F.; Desbat, B.; Lassegues, J. C.; Garie, R. Infrared and Raman spectroscopies of rf sputtered tungsten oxide films. *J. Solid State Chem.* **1988**, *73* (1), 127−139.

(63) Daniel, M. F.; Desbat, B.; Lassegues, J. C.; Gerand, B.; Figlarz, M. Infrared and Raman study of WO3 tungsten trioxides and WO3, xH2O tungsten trioxide tydrates. *J. Solid State Chem.* **1987**, *67* (2), 235−247.

(64) Spitzin, V. I.; Kabanow, V. J. Anwendung von kinetischen Methoden fur die Untersuchung der Struktur und der Reaktionen der Bildung von hochmolekularen Aquowolframaten. *Z. Anorg. Allg. Chem.* **1963**, *322* (5−6), 248−264.

(65) Iglesia, E.; Soled, S. L.; Fiato, R. A. Fischer−Tropsch synthesis on cobalt and ruthenium. Metal dispersion and support effects on reaction rate and selectivity. *J. Catal.* **1992**, *137* (1), 212−224.

(66) Lin, H.-Y.; Chen, Y.-W. The kinetics of H2 adsorption on supported ruthenium catalysts. *Thermochim. Acta* **2004**, *419* (1−2), 283−290.

(67) Ravel, B.; Newville, M. ATHENA, ARTEMIS, HEPHAESTUS: data analysis for X-ray absorption spectroscopy usingIFEFFIT. *J. Synchrotron Radiat.* **2005**, *12* (4), 537−541.

(68) Kresse, G.; Hafner, J. Ab initiomolecular dynamics for liquid metals. *Phys. Rev. B: Condens. Matter Mater. Phys.* **1993**, *47* (1), 558−561.

(69) Kresse, G.; Furthmüller, J. Efficient iterative schemes forab initiototal-energy calculations using a plane-wave basis set. *Phys. Rev. B: Condens. Matter Mater. Phys.* **1996**, *54* (16), 11169−11186.

(70) Kresse, G.; Furthmüller, J. Efficiency of ab-initio total energy calculations for metals and semiconductors using a plane-wave basis set. *Comput. Mater. Sci.* **1996**, *6* (1), 15−50.

(71) Grimme, S.; Antony, J.; Ehrlich, S.; Krieg, H. A consistent and accurate ab initio parametrization of density functional dispersion correction (DFT-D) for the 94 elements H-Pu. *J. Chem. Phys.* **2010**, *132* (15), 154104.

(72) Grimme, S.; Ehrlich, S.; Goerigk, L. Effect of the damping function in dispersion corrected density functional theory. *J. Comput. Chem.* **2011**, *32* (7), 1456−1465.

(73) Kresse, G.; Joubert, D. From ultrasoft pseudopotentials to the projector augmented-wave method. *Phys. Rev. B: Condens. Matter Mater. Phys.* **1999**, *59* (3), 1758−1775.

(74) Held, G.; Menzel, D. The structure of the p($\sqrt{3} \times \sqrt{3}$)R30° bilayer of D2O on Ru(001). *Surf. Sci.* **1994**, *316* (1−2), 92−102.

(75) Salje, E. K.; Rehmann, S.; Pobell, F.; Morris, D.; Knight, K. S.; Herrmannsdörfer, T.; Dove, M. T. Crystal structure and paramagnetic behaviour of. *J. Phys.: Condens. Matter* **1997**, *9* (31), 6563.

(76) Monkhorst, H. J.; Pack, J. D. Special points for Brillouin-zone integrations. *Phys. Rev. B* **1976**, *13* (12), 5188−5192.